Model-based process design of a ternary protein separation using multi-step gradient ion-exchange SMB chromatography

Qiao-Le He^{1, 2, 4}, Zhaoxi Sun³, and Liming Zhao*^{1, 2}

¹State Key Laboratory of Bioreactor Engineering, East China University of Science and Technology, 200237 Shanghai, China

²R&D Center of Separation and Extraction Technology in Fermentation Industry, East China University of Science and Technology, 200237 Shanghai, China ³Forschungszentrum Jülich, IAS-5/INM-9:Computational Biomedicine, 52425 Jülich, Germany

⁴Forschungszentrum Jülich, IBG-1:Biotechnology, 52425 Jülich, Germany

Oct. 10, 2019

Abstract

Model-based process design of ion-exchange simulated moving bed (IEX-SMB) chromatography for center-cut separation of proteins is studied. Use of nonlinear binding models that describe more accurate adsorption behaviours of macro-molecules could make it impossible to utilize triangle theory to obtain operating parameters. Moreover, triangle theory provides no rules to design salt profiles in IEX-SMB. In the modelling study here, proteins (i.e., ribonuclease, cytochrome and lysozyme) on the chromatographic columns packed with strong cation-exchanger SP Sepharose FF is used as an example system. The general rate model with steric mass-action kinetics was used; two closed-loop IEX-SMB network schemes were investigated (i.e., cascade and eight-zone schemes). Performance of the IEX-SMB schemes was examined with respect to multi-objective indicators (i.e., purity and yield) and productivity, and compared to a single column batch system with the same amount of resin utilized. A multi-objective sampling algorithm, Markov Chain Monte Carlo (MCMC), was used to generate samples for constructing the Pareto optimal fronts. MCMC serves on the sampling purpose, which is interested in sampling the Pareto optimal points as well as those near Pareto optimal. Pareto fronts of the three schemes provide the full information of trade-off between the conflicting indicators of purity and yield. The results indicate the cascade IEX-SMB scheme and the integrated eight-zone IEX-SMB scheme have the similar performance that both outperforms the single column batch system.

1 Introduction

Protein purification and separation are major concerns in the downstream processing of pharmaceutical industries (Carta & Jungbauer, 2010; Scopes, 2013). They require a series of processes aimed at isolating single or multiple types of proteins from complex intermediates of process productions. Choosing a purification method, depending on the purpose for which the protein is needed, is a critical issue. Chromatography is a prevailing separation technology. Simulated moving bed (SMB) chromatography (Broughton & Gerhold, 1961) is an excellent alternative to the single column batch chromatography, because of its continuous counter-current operation, its potential to enhance productivities and to reduce solvent consumption (Seidel-Morgenstern et al., 2008; Rajendran et al., 2009). According to the position of the columns relative to the

^{*}Corresponding author. zhaoliming@ecust.edu.cn

ports (*i.e.*, feed, raffinate, desorbent, extract), the process is divided into four zones (*i.e.*, I, II, III, IV), each has a specific functionality in the separations (see Fig. 1).

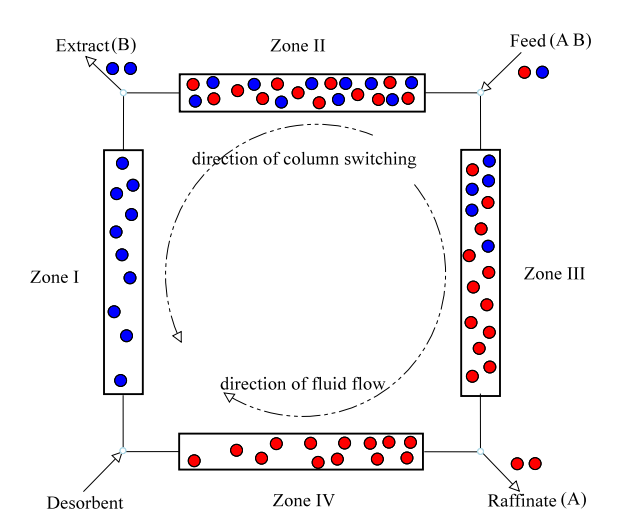


Figure 1: Schematic of four-zone SMB chromatography

Multicolumn continuous chromatography is also commonly used in the protein separation and purification. For instance, there are sequential multicolumn chromatography (SMCC) (Ng et al., 2014), periodic counter-current packed bed chromatography (PCC) (Pollock et al., 2013), gradient with steady state recycle (GSSR) process (Silva et al., 2010), multicolumn solvent gradient purification (MCSGP) (Aumann & Morbidelli, 2007) and capture SMB (Angarita et al., 2015).

However, the prominent features of SMB processes are based on the prerequisite that optimal operating conditions can be determined, which can be very challenging in practice. Determination of operating conditions is predominantly based on classical and extended triangle theories (Storti et al., 1993), which are originally derived from the ideal chromatographic model with linear isotherm. Powerful criteria to design processes with nonlinear isotherms (e.g., Langmuir and Bi-Langmuir) have been elaborated in the past few years (Charton & Nicoud, 1995; Mazzotti et al., 1997; Antos & Seidel-Morgenstern, 2001). Versatile results on triangle theory for the design of SMB processes have been published (Nowak et al., 2012; Kim et al., 2016; Lim, 2004; Kazi et al., 2012; Bentley & Kawajiri, 2013; Bentley et al., 2014; Sreedhar et al., 2014; Toumi et al., 2007; Silva et al., 2015; Kiwala et al., 2016).

Substances separated by SMB processes have recently been evolved from monosaccharides to proteins and other macro-molecules. The adsorption behaviors of macro-molecules, as observed both in experiments (Clark et al., 2007) and molecular dynamic simulations (Dismer & Hubbuch, 2010; Liang et al., 2012; Lang et al., 2015), are much more complex than that described by the linear isotherm, the Langmuir kinetics or the steric mass-action (SMA) model (Brooks & Cramer, 1992). Macro-molecules can undergo conformation changes in the mobile phase, orientation changes on the functional surfaces of stationary phase and aggregation in the whole process. Clark et al. (2007) used an acoustically actuated resonant membrane sensor to monitor the changes of surface energy and found that the changes persist long after mass loading of the protein has reached the steady state. Therefore, more sophisticated adsorption models, such as the multi-state SMA (Diedrich et al., 2017) based on the spreading model (Ghosh et al., 2013, 2014), have been proposed to describe dynamic protein-ligand interactions. Although these kinetics describe more accurately the adsorption behaviors by taking orientation changes into consideration, the strong nonlinearity of kinetics exerts tremendous difficulties in deriving analytical formulae to calculate flowrates, as it is in the triangle theory.

Ion-exchange (IEX) mechanism is commonly used to separate charged components in chromatography. In IEX chromatography (both single column and SMB processes), an auxiliary component acting as a modifier is used to change the electrostatic interaction force between functional groups and macro-molecules; sodium

chloride is most frequently used. The higher the salt concentration is, the lower electrostatic force is, such that the binding affinity is decreased and bounded components are successively eluted (Lang et al., 2015). In the single column IEX processes, this principle can be either implemented in an isocratic mode or a linear gradient mode. The linear gradient mode has frequently been applied to achieve better separation capability (Osberghaus et al., 2012b). While in the IEX-SMB processes, the isocratic mode (i.e., the salt strength is identical in all zones) was originally applied. The gradient mode can be applied, by using a salt strength in the desorbent stream that is stronger than that in the feed (cf. Fig. 1). Thus, high salt concentration in zone I and II (high salt region), low salt concentration in zone III and IV (low salt region). As shown in the studies, applying the gradient mode can further improve the separation performance (Antos & Seidel-Morgenstern, 2001; Houwing et al., 2002, 2003; Li et al., 2007). The salt profiles of the gradient mode are referred to as two-step salt gradient in this work; and derivations of multi-step gradient to ternary separations are intuitive. However, the construction of the multi-step salt gradient imposes difficulty on the design of IEX-SMB processes.

The difficulty can be detoured by using the open-loop multicolumn chromatography, where it is possible to apply linear salt gradients. The open-loop feature and possibility of linear gradient make the application potential of multicolumn continuous chromatography in the downstream processing unarguable (Faria & Rodrigues, 2015). As dealing with the model complexity induced by linear gradients is much easier than that by multi-step ones; moreover, the open-loop feature renders more degrees of freedom in the process designs.

Conventional four-zone SMB processes are tailored for binary separations. Ternary separations are requested in many applications; the selection of network configurations is application-specific. Ternary separations, also referred to as center-cut separations, can be achieved by cascading two four-zone SMB units (Wooley et al., 1998; Nicolaos et al., 2001; Nowak et al., 2012). Cascade schemes require designing and operating two four-zone SMB processes, which can be laborious and costly. Hence, integrated schemes have been developed using a single multi-port valve and fewer pumps than cascade schemes (Seidel-Morgenstern et al., 2008; da Silva & Seidel-Morgenstern, 2016). Moreover, process design is simplified due to simultaneous switching of all columns. Due to the complexity of network configurations, in addition to the kinetic nonlinearity and multi-step gradient, a comprehensive column model, fast numerical solver and efficient optimizer are required.

In this study, we shall present a model-based process design of IEX-SMB units for separating a protein mixture of ribonuclease, cytochrome and lysozyme, using cation-exchange columns packed with SP Sepharose FF beads. Two network configurations for the ternary separation will be used, that is, a cascade scheme and an eight-zone scheme. For comparison, a conventional single column batch system, with the same column geometry and resin utilization, will be studied. In this study, SMB processes are modeled by weakly coupling individual models of the involved columns, *i.e.*, one large equation system is set up and sequentially solved (He et al., 2018). The code has been published as open-source software, CADET-SMB.

The operating conditions of the network configurations will be optimized by a stochastic algorithm, Markov Chain Monte Carlo (MCMC), with respect to conflicting objectives of purity and yield. Pareto fronts are computed for illustrating the best compromises between the two conflicting performance indicators. Unlike multi-objective optimization algorithms (e.g., non-dominated sorted genetic algorithm, strength Pareto evolutionary algorithms) that try to eliminate all the non-dominated points during optimization, MCMC serves on the sampling purpose, which is interested in sampling the Pareto optimal points as well as those near Pareto optimal. For samping purpose, MCMC not only accepts proposals with better objective value, but also accepts moves heading to non-dominated points with certain probability. Therefore, MCMC renders greater information for process design. Besides, uncertainties of parameters that is related to the robustness of process design can be examined, though the information is not involved in this study. As shown in the Pareto fonts, the performance indicators of the single column are dominated by that of both cascade and eight-zone schemes. The performances of the two IEX-SMB schemes are quite similar, though the cascade scheme has a slight advantage over the eight-zone scheme.

2 Theory

This section introduces the transport model, binding kinetics, load-wash-elution mode of the single column, SMB network connectivity, performance indicators and optimization algorithm.

2.1 Transport model

The transport behavior of proteins in the column is described by means of the general rate model (GRM), which accounts for various levels of mass transfer resistance (Guiochon et al., 2006).

GRM considers convection and axial dispersion in the bulk liquid, as well as film mass transfer and pore diffusion in the porous beads:

$$\frac{\partial c_i^j}{\partial t} = -u_{\text{int}}^j \frac{\partial c_i^j}{\partial z} + D_{\text{ax}}^j \frac{\partial^2 c_i^j}{\partial z^2} - \frac{1 - \varepsilon_c}{\varepsilon_c} \frac{3}{r_p} k_{f,i}^j \left(c_i^j - c_{p,i}^j (r = r_p) \right)$$
(1a)

$$\frac{\partial c_{p,i}^{j}}{\partial t} = D_{p,i}^{j} \left(\frac{\partial^{2} c_{p,i}^{j}}{\partial r^{2}} + \frac{2}{r} \frac{\partial c_{p,i}^{j}}{\partial r} \right) - \frac{1 - \varepsilon_{p}}{\varepsilon_{p}} \frac{\partial q_{i}^{j}}{\partial t}$$
(1b)

where c_i^j , $c_{p,i}^j$ and q_i^j denote the interstitial, stagnant and stationary phase concentrations of component $i \in \{1, ..., M\}$ in column $j \in \{1, ..., N\}$. Furthermore, $z \in [0, L]$ denotes the axial position where L is the column length, $r \in [0, r_p]$ is the radial position, r_p is the particle radius, t time, ε_c column porosity, ε_p particle porosity, u_{int}^j interstitial velocity, D_{ax}^j is the axial dispersion coefficient, $D_{p,i}^j$ the effective pore diffusion coefficient, and $k_{f,i}^j$ the film mass transfer coefficient. At the column inlet and outlet, Danckwerts boundary conditions (Barber et al., 1998) are applied:

$$\begin{cases}
\frac{\partial c_i^j}{\partial z} \Big|_{z=0} &= \frac{u_{\text{int}}^j}{D_{\text{ax}}^j} \left(c_i^j(z=0) - c_{\text{in},i}^j \right) \\
\frac{\partial c_i^j}{\partial z} \Big|_{z=L} &= 0
\end{cases}$$
(2)

where $c_{\text{in},i}^{j}$ is the inlet concentration of component i in column j; the calculation of inlet concentration in SMB chromatography is deferred to Eq. (7). The boundary conditions at the particle surface and center are given by:

$$\begin{cases}
\frac{\partial c_{p,i}^{j}}{\partial r}\Big|_{r=r_{p}} &= \frac{k_{f,i}^{j}}{\varepsilon_{p}D_{p,i}^{j}} \left(c_{i}^{j} - c_{p,i}^{j}(r=r_{p})\right) \\
\frac{\partial c_{p,i}^{j}}{\partial r}\Big|_{r=0} &= 0
\end{cases} \tag{3}$$

2.2 Binding kinetics

The steric mass-action (SMA) model has been widely reported for predicting and describing nonlinear ion-exchange adsorption of proteins; the relationship between the stagnant liquid $c_{p,i}^{j}$ and the stationary phase q_{i}^{j} is described as follows:

$$\frac{\mathrm{d}q_i^j}{\mathrm{d}t} = k_{a,i} \, c_{p,i}^j \, (\bar{q}_0^j)^{\nu_i} - k_{d,i} \, q_i^j \, (c_{p,0}^j)^{\nu_i} \tag{4}$$

where $k_{a,i}$ and $k_{d,i}$ denote adsorption and desorption coefficients, ν_i is the characteristic charge of the adsorbing molecules, and σ_i the shielding factor. c_0 , $c_{p,0}$, q_0 denote the salt concentration in the three

different phases. Moreover, \bar{q}_0 denotes counter ions that are not shielded and available for protein binding,

$$\bar{q}_0 = q_0 - \sum_{i=1}^{M} \sigma_i q_i \tag{5}$$

It can be expressed with electro-neutrality condition,

$$\bar{q}_0 = \Lambda - \sum_{i=1}^{M} (\nu_i + \sigma_i) q_i \tag{6}$$

where Λ is the ionic capacity.

2.3 Single column batch system

There are various possibilities to operate a single column in batch manner. The specific one described here is used for comparison with SMB processes; we refer you the protocol to Osberghaus et al. (2012b). Apart from regeneration steps, an operating cycle of the single column could consist of three phases: load, wash and elution, see Fig. 2. In phase I, the column is equilibrated with the running buffer, then the protein solution is injected to the column for a t_{load} time. It is then followed by a wash step (II), that is, pumping through the column with running buffer for a t_{wash} time. Afterwards, gradient modes (involving zero gradient) are set to elute the bounded protein for a t_{elute} time. Elution (III) can be implemented by multi-step solvent gradients. As depicted in Fig. 2 as an example, there are two parts (*i.e.*, IIIa, IIIb) with linear gradients but different slopes (m_1 , m_2), and eventually an isocratic part (IIIc). Multi-step gradients are used, because in center-cut separations peak overlaps at the front and at the back of the target component need to be minimized. With the regeneration of the column (IV), it comprises an operating cycle of the single.

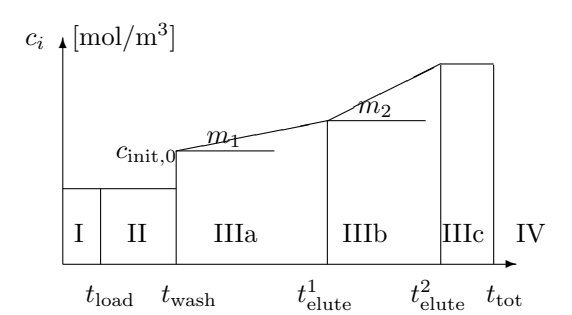


Figure 2: Sequential phases of single column gradient elution chromatography. I: load phase; II: wash phase; III: multi-step elution phase; IV: regeneration.

2.4 SMB network connectivity

In SMB chromatography two adjacent columns, j and j+1, are connected via a node j, see Fig. 3. A circular SMB loop is closed when two column indices point to the same physical column (i.e., by identifying column j = N+1 with column j = 1), see Fig. 1. In this work, node j is located at the downstream side of column j and upstream of column j+1. At each node only one or none of the feed (F), desorbent (D), raffinate (R), or extract (E) streams exists at a time. The inlet concentration of component i in column j+1 is calculated from mass balance of the node j:

$$c_{\text{in},i}^{j+1} = \frac{c_{\text{out},i}^{j} Q^{j} + \delta_{i}^{j}}{Q^{j+1}}$$
 (7)

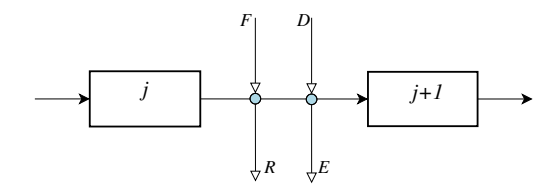


Figure 3: Schematic of network connection between two adjacent columns.

where $c_{\text{out},i}^j = c_i^j(t,z=L)$ denotes the outlet concentration of component i in column j, $Q^j = \varepsilon_c u_{\text{int}}^j \pi d_c^2/4$ the volumetric flowrates and d_c the column diameter. Meanwhile, δ^j determines the current role of node j (i.e., F, D, R, E or none):

$$\delta_{i}^{j} = \begin{cases} c_{\text{in,i}}^{F} Q^{F} & \text{feed} \\ c_{\text{in,i}}^{D} Q^{D} & \text{desorbent} \\ -c_{\text{out,i}}^{j} Q^{R} & \text{raffinate} \\ -c_{\text{out,i}}^{j} Q^{E} & \text{extract} \\ 0 & \text{none} \end{cases}$$
(8)

where $c_{\rm in}^F$ and $c_{\rm in}^D$ are the component concentrations at feed and desorbent ports, and Q^F , Q^D , Q^R , Q^E the volumetric flowrates at the feed, desorbent, raffinate, and extract ports, respectively. $\delta^j = 0$ indicates nodes that are currently not connected to a port (*i.e.*, in the interior of a zone); this occurs when more columns than zones are present, such as eight columns in a four-zone scheme. As there might be multiple feed, desorbent, raffinate, and extract ports in SMB processes (*e.g.*, the cascade scheme and the integrated eight-zone scheme), an extension of the indexing scheme is required. Column shifting is implemented by periodically permuting δ each switching time t_s .

2.5 Performance indicators

Purity, yield and productivity are commonly used for evaluating the performance of chromatographic processes. All indicators can be defined within one collection time t_c (Bochenek et al., 2013). In the case of SMB systems, t_c is the switching time t_s , while in single column systems it is the length of pooling time interval t_n .

In this study, performance indicators are all defined in terms of component, $i \in \{1, ..., M\}$, withdrawn at a SMB node, $j \in \{E, R, ...\}$, or collected at the outlet of single column systems, $j \in \{B\}$, within the pooling interval. The definitions of performance indicators are all based on concentration integrals $A^j_{\text{out},i}$ of component i at node j,

$$A_{\text{out},i}^{j} = \int_{t-\tau}^{\tau+t_{c}} c_{i}^{j}(t, z = L) \, \mathrm{d}t$$
 (9)

In SMB, τ is the starting time of one switching interval and all performance indicators are calculated when the system is upon cyclic steady state (CSS); it is the starting point of the pooling time interval in single column.

The purity, Pu_i^j , is the concentration integral of component *i* relative to the integral sum of all components, Eq. (10). The yield, Y_i^j , is the ratio of the withdrawn mass and the feed mass, Eq. (11).

$$Pu_i^j = \frac{A_{\text{out},i}^j}{\sum_{k=1}^M A_{\text{out},k}^j}$$
 (10)

$$\mathbf{Y}_{i}^{j} = \frac{Q^{j} A_{\text{out},i}^{j}}{Q^{F} c_{\text{in},i}^{F} t_{\text{load}}}$$
(11)

In SMB, when the solution stream is continuously fed via the feed node and the extracts and raffinates are continuously withdrawn, $t_{\text{load}} = t_s = t_c$ and Q^F differs with Q^j . While in the single column, the flowrates are the same at the inlet node and outlet node, $Q^j = Q^F$; and $t_{\text{load}} \neq t_p = t_c$. The productivity, \Pr_i^j , is the withdrawn mass of the component i per collection time relative to the total volume of the utilized packed bed in all columns,

$$\Pr_{i}^{j} = \frac{Q^{j} A_{\text{out},i}^{j}}{t_{c} (1 - \varepsilon_{c}) V_{c} N}$$
(12)

In single column systems, N=1. According to the definitions of \Pr_i^j and Υ_i^j , both indicators increase with increasing amounts of the product collected, *i.e.*, $A_{\text{out},i}^j$. However, \Pr_i^j can also be improved by reducing the collection time t_c .

2.6 Optimization

Generally, operating conditions of both SMB and single column processes are systematically optimized by numerical algorithms such that the above performance indicators are all maximized. In studies of center-cut separations, the middle component i is of interest. To specifically account for a vector of the conflicting performance indicators of $[Pu_i^j, Y_i^j]$ (referred to as \mathcal{PI} hereafter) in this study, multi-objective optimization is applied.

A set of objectives can be combined into a single objective by adding each objective a pre-multiplied weight (the weighted method (Marler & Arora, 2010)), or keeping just one of the objectives and with the rest of the objectives constrained (the ε -constraint method (Mavrotas, 2009)). The latter method is used in this work, that is, maximizing the yield of the target component of the processes with the purity constrained to be larger than a threshold ε_i^j :

min
$$f(\theta) = -\mathbf{Y}_{i}^{j}$$

s.t.
$$\begin{cases} c_{i}(\theta) : \mathbf{P}\mathbf{u}_{i}^{j} - \varepsilon_{i}^{j} \geqslant 0 \\ \theta_{\min} \leqslant \theta \leqslant \theta_{\max} \end{cases}$$
(13)

where θ is a vector of optimized parameters with boundary limitations of $[\theta_{\min}, \theta_{\max}]$. The inequality $c_i(\theta)$ is lumped into the objective function using penalty terms in this study, such that it can be solved as a series of unconstrained minimization problems with increasing penalty factors, σ_k ,

$$\min \mathcal{H}(\theta; \sigma_k) = f(\theta) + \sigma_k g(\theta) \tag{14}$$

In Eq. (14), the penalty function is chosen as $g(\theta) = \|\min\{0, c(\theta)\}\|^2$.

Different types of methods can be applied to solve the minimization of $\mathcal{H}(\theta; \sigma_k)$, such as deterministic methods and heuristic methods. Additionally, stochastic methods can be chosen. In order to use a stochastic method, the minimization of $\mathcal{H}(\theta; \sigma_k)$ is further formulated to maximum likelihood estimation:

$$\arg \max_{\theta} \mathcal{L}(\theta) \tag{15}$$

where the likelihood is defined as an exponential function of $\mathcal{H}(\theta; \sigma_k)$:

$$\mathcal{L}(\theta) \stackrel{\text{def}}{=} \exp\left[-\frac{1}{2}\mathcal{H}(\theta; \sigma_k)\right] \tag{16}$$

2.7 Numerical solution

All numerical simulations were computed on an Intel(R) Xeon(R) system with 16 CPU cores (64 threads) running at 2.10 GHz.

The mathematical models described above for each column of SMB processes are weakly coupled together and then iteratively solved. The open-source code has been published on Github, https://github.com/modsim/CADET-SMB.git. CADET-SMB repeatedly invokes CADET kernel to solve each individual column

model, with default parameter settings. CADET is also an open-source software published on Github, https://github.com/modsim/CADET.git. The axial column dimension is discretized into $N_z = 40$ cells, while the radical bead is discretized into $N_r = 10$ cells. The resulting system of ordinary differential equations is solved using an absolute tolerance of 10^{-10} , relative tolerance of 10^{-6} , an initial step size of 10^{-14} and a maximal step size of $5 \cdot 10^{6}$.

A stochastic multi-objective sampling algorithm, MCMC, is applied in this study to optimize the operating conditions. Specifically, the Metropolis-Hastings algorithm, incorporating with delayed rejection, adjusted Metropolis and Gibbs sampling, has been published as open-source software on Github, https://github.com/modsim/CADET-MCMC.git. For sampling purpose, MCMC not only accepts proposals with better objective values, but also accepts moves heading to non-dominated points with certain probability. Samples are collected until the Geweke convergence criterion (Geweke et al., 1991) is smaller than 10^{-4} or the desired sample size is reached.

The Pareto fronts in this study describe two-dimensional trade-offs between purity and yield. Thus, non-dominated stable sort method of Pareto front were is applied to generate the frontiers (Duh et al., 2012).

3 Case

A protein mixture of ribonuclease, cytochrome and lysozyme is of interest in this study, $i \in \{\text{RNase, cyt, lyz}\}$. It is a prototype example used in the academic field for modelling purposes (Osberghaus et al., 2012a,b). The fractionation of this protein mixture is also referred to as center-cut separation, that is, the center component, cyt, is targeted and the other two components are regarded as impurities in separations. In the modelling study here, we have used the proteins on chromatographic columns packed with strong cation-exchanger SP Sepharose FF as an example system (see the column geometry in Tab. 1).

Catalogue	Symbol	Description	Value	Unit
	L	column length	1.4×10^{-2}	m
	d_c	column diameter	1×10^{-2}	m
Geometry	d_p	particle diameter	9.00×10^{-5}	m
	ε_b	column porosity	0.37	
	ε_p	particle porosity	0.75	
	$D_{\rm ax}$	axial dispersion	5.75×10^{-8}	${\rm m}^2{\rm s}^{-1}$
Transport	D_p	pore diffusion	6.07×10^{-11}	${ m m}^2{ m s}^{-1}$
	$k_f^{'}$	film mass transfer	6.90×10^{-6}	${ m ms^{-1}}$
	Λ	ionic capacity	1200	$\mathrm{mol}\mathrm{m}^{-3}$
Kinetics	$k_{\mathrm{eq},i}$	equilibrium constant	$[7.70, 1.59, 35.5] \times 10^{-3}$	
Killetics	ν_i	characteristic charges	[3.70, 5.29, 4.70]	
	σ_i	steric factors	[10.0, 10.6, 11.83]	

Table 1: Parameters of geometry, transport and binding kinetics of RNase, cyt and lyz.

Simplified models (e.g., TDM and EDM) that rely on an assumption of equal concentrations in the particle pores and in the mobile phase, can not been applied here; because mass transfer dynamics of macro-molecules in ca. 100 µm beads can be rate limiting (Lodi et al., 2017). Hence, the GRM model is used to describe the mass transfer in porous beads. In addition, the SMA model inherently considers the impact of salt on binding affinity, the hindrance effect of macro-molecules. The mathematical modelling of the prototype example has been presented in Teske et al. (2006) and Püttmann et al. (2013); the transport and binding parameters from experiments are shown in Tab. 1. The geometry, transport and binding parameters are directly used in this study; and the operating conditions will be optimized.

In the pharmaceutical manufacturing usually at least 99% purity of cyt is needed. Therefore, taking expensive computation cost in IEX-SMB simulations to generate Pareto optimal points with lower purities is also a trade-off. In this study, the $\varepsilon_{\rm cyt}^j$ in Eq. 13 is set to 99%; thus, only the Pareto optimal fragment with purity higher than 99% is concerned in IEX-SMB. This implementation reduces the heavy computational

burden of multi-objective sampling, as much fewer samples are requested to construct the frontiers. Pareto optimal fragment can be further extended by repeatedly solving Eq. (15) with varying values of $\varepsilon_{\text{cyt}}^j$. However, in the single column the whole Pareto optimal front is concerned as the computational cost is not expensive. This can be one of the advantages of the ε -constraint method.

3.1 Single column

In the single column system, the equilibration, load-wash-elution and regeneration phases are performed. The interstitial velocity is $5.75 \cdot 10^{-4}\,\mathrm{m\,s^{-1}}$; the retention time for a non-retained component is $24.35\,\mathrm{s}$. $1\,\mathrm{mol\,m^{-3}}$ concentration of RNase, cyt and lyz is injected in the load phase. In both the load and wash steps, a salt concentration of $50\,\mathrm{mol\,m^{-3}}$ is applied. The operating time intervals for the load and wash phases are $10\,\mathrm{s}$ and $40\,\mathrm{s}$. The shapes of the multi-step elution phase, that can be characterized by the bilinear gradients (i.e., m_1 and m_2), the operating time intervals, and the initial salt concentration (i.e., $c_{\mathrm{init},0}$), are optimized. Since the symbols as illustrated in Fig. 2 are the elapsed times, the operating time intervals are calculated (i.e., $\Delta t_1 = t_{\mathrm{elute}}^1 - 50$ and $\Delta t_2 = t_{\mathrm{elute}}^2 - t_{\mathrm{elute}}^1$). Thus, the optimized operating parameters are $\theta = \{\Delta t_1, \Delta t_2, m_1, m_2, c_{\mathrm{init},0}\}$.

3.2 SMB

Depending on initial states, SMB processes often undergoes a ramp-up phase and eventually enter into a CSS. In this study, the system is assumed to be upon CSS when a difference between two iterations (k, k+1) falls below a predefined tolerance error, e_t , see Eq. (17).

$$\max_{j \in \{R, E\}} \sum_{i=1}^{M} \left(\int_{0}^{t_{s}} \left| c_{i,k}^{j}(t, z = L) - c_{i,k+1}^{j}(t, z = L) \right|^{n} dt \right)^{\frac{1}{n}} \leq e_{t}$$
 (17)

In this study, the columns of IEX-SMB are initially empty except for the concentration of bound salt ions q_0 that is set to the ionic capacity Λ , in order to satisfy the electro-neutrality condition. Additionally, the initial salt concentrations in column j, $c_0^j(t=0,z)$, $c_{p,0}^j(t=0,z)$, $q_0^j(t=0,z)$, are set equal to the salt concentrations in the upstream inlet nodes. Taking the four-zone scheme as an example (cf. Fig. 1), the salt concentrations of the mobile and stationary phases (c_0^j and $c_{p,0}^j$) in zone III and IV are set to the value of c_0^F ; while c_0^j and $c_{p,0}^j$ in zone I and II are set to the value of c_0^D :

$$\begin{cases} c_0^j(t=0,z) = c_{p,0}^j(t=0,z) = c_0^D & j \in \{\text{I},\text{II}\} \\ c_0^j(t=0,z) = c_{p,0}^j(t=0,z) = c_0^F & j \in \{\text{III},\text{IV}\} \\ q_0^j(t=0,z) = \Lambda & j \in \{\text{I},\text{II},\text{III},\text{IV}\} \end{cases}$$
(18)

In contrast to the single column system, the chosen initial state of SMB processes is irrelevant to the performance indicators calculated upon CSS.

A cascade of two four-zone units (named as U_1 and U_2 in the following content) and an integrated eight-zone scheme are applied, see Fig. 4. In both schemes, three single columns in each zone and 24 columns at all are designed. In this study, the volumetric flowrate of zone I is defined as recycle flowrate, Q^{rec} . In each sub-unit of the cascade scheme, the optimized operating parameters are the switching time (same for both units as they are synchronously switched), recycle flowrate, the inlet and outlet flowrates, and the salt concentrations at the inlet ports, $\theta = \{t_s, [Q^{\text{rec}}]_{U_1}, [Q^D]_{U_1}, [Q^E]_{U_1}, [Q^F]_{U_1}, [c_0^F]_{U_1}, [c_0^D]_{U_1}, [Q^{\text{rec}}]_{U_2}, [Q^D]_{U_2}, [Q^D$

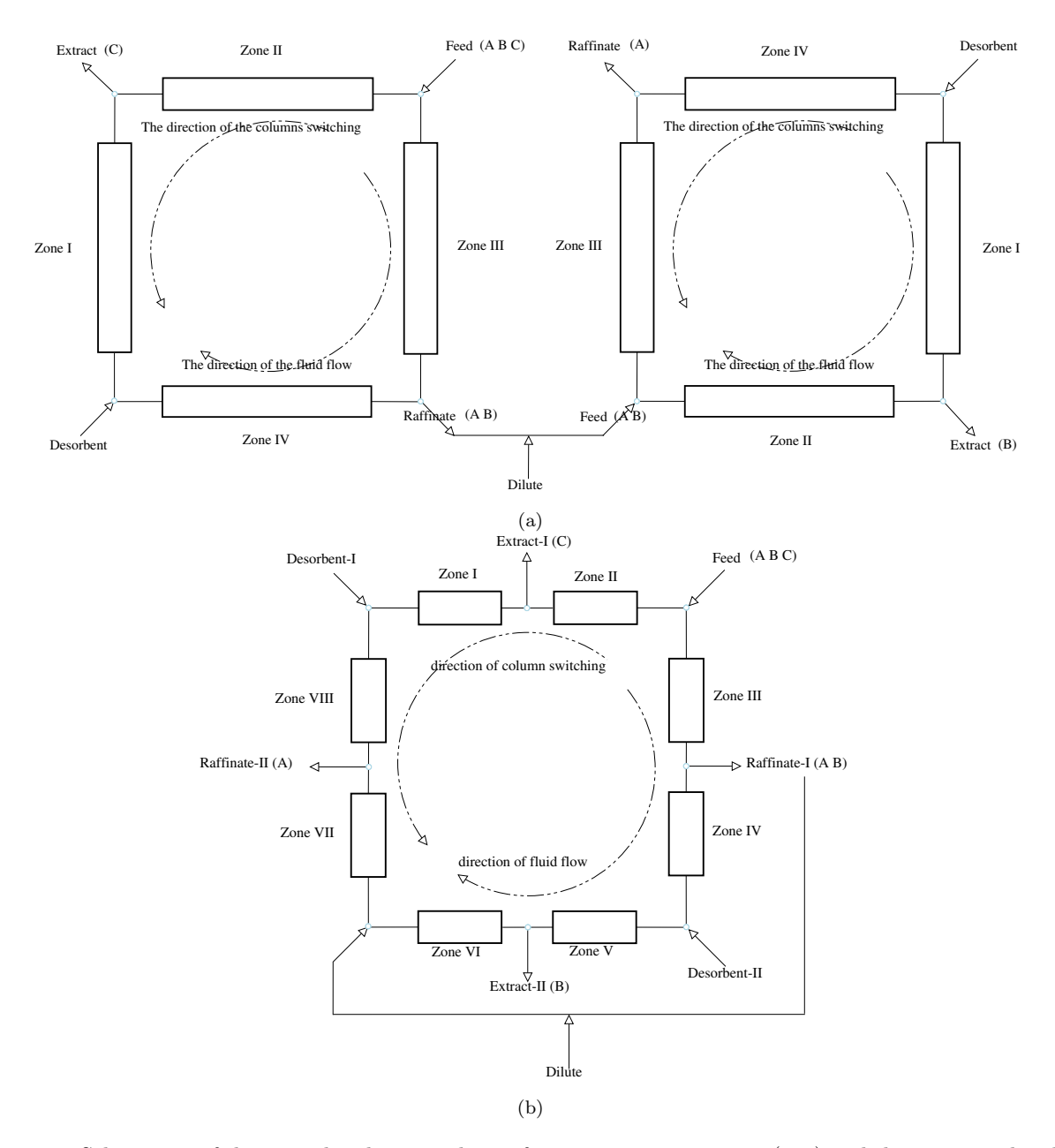


Figure 4: Schematics of the cascade scheme with two four-zone IEX-SMB units (top) and the integrated eight-zone scheme (bottom) applied in this study for ternary separations. In each zone, there can be multiple columns.

Table 2: Searching domain for the design of the single column system.

Symbol	Description -	Val	Unit	
Symbol	Description -	min	max	- Ont
Δt_1	elution interval one	500	8000	s
Δt_2	elution interval two	1000	8000	s
m_1	elution gradient one	$1.0 \cdot 10^{-3}$	$1.0 \cdot 10^{-2}$	
m_2	elution gradient two	$1.0 \cdot 10^{-3}$	20	
$c_{ m init,0}$	initial salt conc.	20	200	$\mathrm{mol}\mathrm{m}^{-3}$

4 Results and discussion

4.1 Single column

The gradient shapes of the single column process are first optimized in order to have a comparison with the IEX-SMB processes. Searching domain of the parameters, θ , is listed in Tab. 2. The intervals are based on literature values with additional safety margins. The maximal sampling length here is $1.2 \cdot 10^4$ and the burn-in length is set to 50% of the samples. Fig. 5 shows the Pareto optimal front between purity and yield, as computed by Eq. (10) and Eq. (11). At a rather low purity requirement of 85%, a yield of 0.9 can be achieved. However, at purity of 98%, the yield drops dramatically to 0.1. The Pareto front provides full information of the single column process; the corresponding operating conditions, that render the Pareto optima on demand in application, can be chosen on purpose.

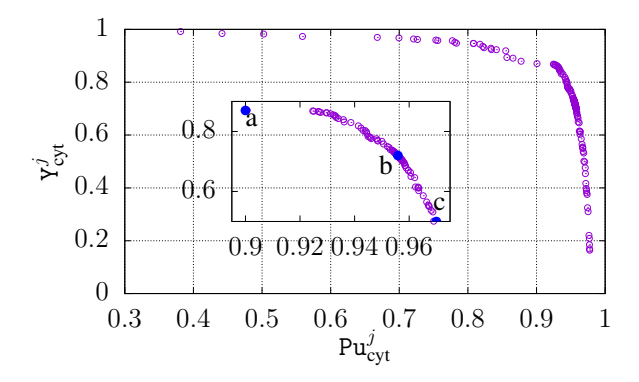


Figure 5: Pareto optimal front of the yield and purity performance indicators in the single column system.

Three characteristic points (i.e., a, b, c) on the above Pareto front are exemplified and then compared. In Fig. 6, the corresponding chromatograms and multi-step salt gradients are shown; the grey areas indicate the pooling time intervals, t_p , of the target components. The calculated performance indicators of the three characteristic points are as follows: $\mathcal{PI}^B_{\rm cyt} = [\mathtt{Pu}^B_{\rm cyt}, \mathtt{Y}^B_{\rm cyt}]$ is [90.0%, 0.85], and the productivity is $\mathtt{Pr}^B_{\rm cyt} = 4.94 \cdot 10^{-3} \, \mathrm{mol} \, \mathrm{m}^{-3} \, \mathrm{s}^{-1}$ of the point a (see Fig. 6a). While they are [95.59%, 0.71] and $7.98 \cdot 10^{-5} \, \mathrm{mol} \, \mathrm{m}^{-3} \, \mathrm{s}^{-1}$ of the point b (see Fig. 6b), [97.02%, 0.49] and $1.36 \cdot 10^{-4} \, \mathrm{mol} \, \mathrm{m}^{-3} \, \mathrm{s}^{-1}$ of the point c (see Fig. 6c). The respective operating parameters are listed in Tab. 3.

The pooling time length $t_p = 5808 \,\mathrm{s}$ in Fig. 6b is much bigger than that in Fig. 6a (i.e., 112 s) and Fig. 6c (i.e., 2352 s). In this study, pooling time intervals were calculated from that the concentrations of other two components (i.e., RNase and lyz) are lower than a predefined threshold, $\mu = 7.5 \cdot 10^{-5}$. Based on the same operating parameters, if we set μ to a larger value, higher yield and lower purity will be obtained. Therefore, the selection is also a trade-off, which is illustrated in a Pareto front in Fig. 7, where μ was decreased from 10^{-4} to $2.5 \cdot 10^{-5}$ with equivalent gap of $2.5 \cdot 10^{-5}$ using operating parameters listed in the b column of Tab. 3.

Shorter pooling time interval means the cyt peak is more stiffly concentrated; it can result in high yield

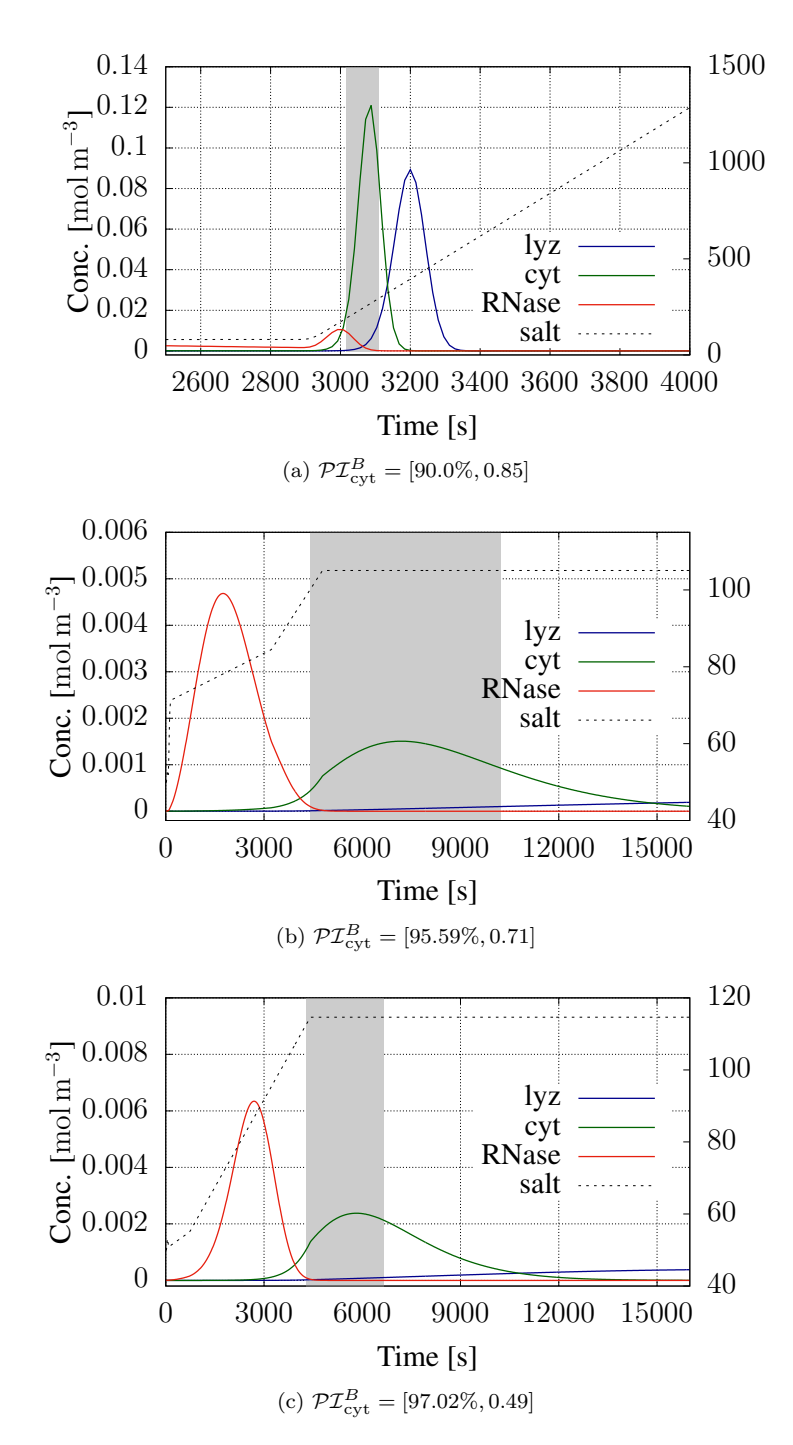


Figure 6: Chromatograms of the single column system (solid lines) and the corresponding multi-step elution gradients (dashed lines).

Table 3: Operating parameters of points a, b, c in the single column system.

θ	a	b	c	
Δt_1	$2.81 \cdot 10^3$	$3.12 \cdot 10^3$	$6.26 \cdot 10^{2}$	s
Δt_2	$3.53 \cdot 10^{3}$	$1.56 \cdot 10^{3}$	$3.68 \cdot 10^{3}$	s
m_1	$1.28 \cdot 10^{-3}$	$4.29 \cdot 10^{-3}$	$6.47 \cdot 10^{-3}$	
m_2	1.11	$1.32 \cdot 10^{-2}$	$1.62 \cdot 10^{-2}$	
$c_{ m init,0}$	77.2	71.7	51.0	$\rm molm^{-3}$

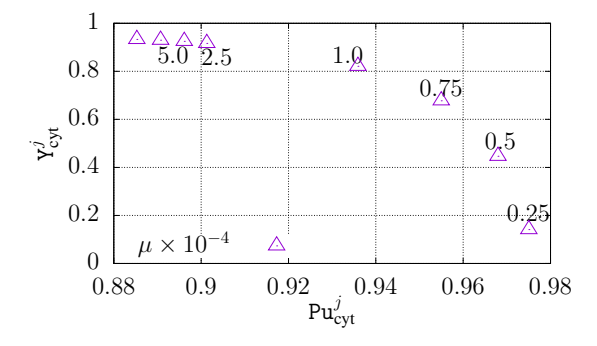


Figure 7: Impact of ϵ values on the trade-off relationship of purity and yield. μ is decreased from 10^{-4} to $2.5 \cdot 10^{-5}$ with equivalent gap of $2.5 \cdot 10^{-5}$.

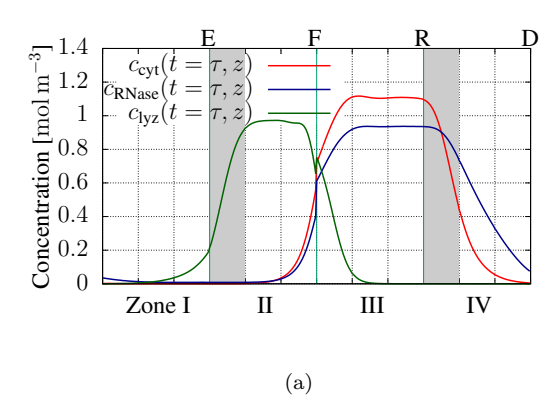
but larger overlap areas (thus low purity) as a conflict, see Fig. 6a. When pooling time interval is longer, the cyt peak is more spread and it renders relatively lower yield but higher purity, see Fig. 6b. As observed in Fig. 6, the peak of cyt always overlaps with the other two peaks, rather than thoroughly separated. In Fig. 6b and 6c, even when lyz is hardly washed out, it begins to be eluted out with small concentration values quite early. Additionally, as lyz is almost not eluted out in Fig. 6b and 6c, a strip step is needed before the regeneration step, in order to make the column reusable. The overlaps may denotes that cyt can not be collected with 100% purity with the single column batch system.

4.2 Cascade scheme

Numerical optimization of the IEX-SMB schemes require suitable initial values. To this end, empirical rules have been developed with big efforts to achieve the center-cut separation first. With the operating conditions listed in the *empirical* column of Tab. 6, lyz is collected at the R port of U_1 with $[\mathcal{PI}_{\text{lyz}}^R]_{U_1} = [98.23\%, 0.99]$ (see Fig. 8a). In U_2 , cyt spreads towards the R port of U_2 , resulting low yield at the E port (i.e., $[Y_{\text{cyt}}^E]_{U_2} = 0.33$) and low purity at the R port (i.e., $[Pu_{\text{RNase}}^R]_{U_2} = 58.39\%$) (the chromatogram is not shown). Based on the initial values with safety margins, searching domain as shown in Tab. 4 is used for numerical optimization. SMB processes often undergo a long ramp-up phase first and eventually enter into a CSS. Elaborately

Table 4: Boundary conditions of the operating parameters of the cascade scheme.

Symbol	Description -	Value	Unit	
Symbol	Description —	min	max	· Omi
$Q^{\rm rec}$	recycle flowrate	$2.06 \cdot 10^{-8}$	$3.06 \cdot 10^{-8}$	${ m m}^{3}{ m s}^{-1}$
Q^F	feed one flowrate	$0.84 \cdot 10^{-8}$	$1.84 \cdot 10^{-8}$	${ m m}^{3}{ m s}^{-1}$
Q^D	desorbent one flowrate	$0.69 \cdot 10^{-8}$	$1.69 \cdot 10^{-8}$	${ m m}^{3}{ m s}^{-1}$
Q^E	extract one flowrate	$0.35 \cdot 10^{-8}$	$1.25 \cdot 10^{-8}$	${ m m}^{3}{ m s}^{-1}$
c_0^F	feed two salt conc.	180	220	$\rm molm^{-3}$
$Q^E \ c_0^F \ c_0^D$	desorbent two salt conc.	220	260	$\mathrm{mol}\mathrm{m}^{-3}$



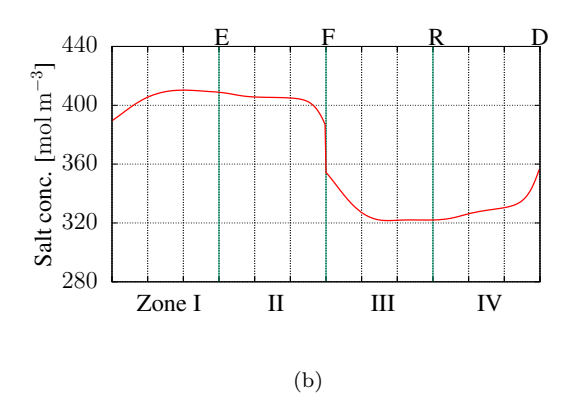


Figure 8: Left: Chromatograms of the first sub-unit in the cascade IEX-SMB upon CSS from the empirical design (left). Right: Salt profiles, $c_0(t, z)$, along the columns of the first sub-unit upon the CSS $(t = \tau)$

.

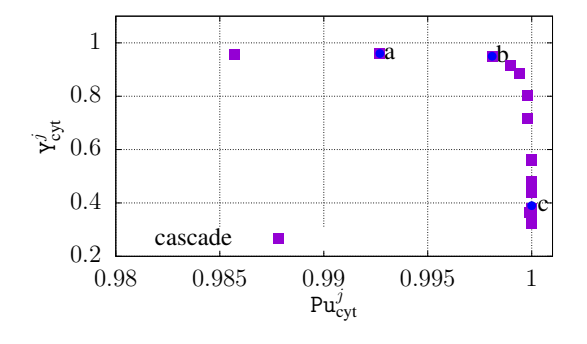


Figure 9: Pareto front of the purity and yield performance indicators of the cascade scheme.

choosing the initial state of columns can also accelerate the convergence (Bentley et al., 2014). In this case, a total of ca. k = 108 switches was required for each IEX-SMB simulation to fall below the tolerance error of $e_t = 10^{-5}$, see Eq. (17). Thus, gaining points for generating Pareto fronts in SMB chromatographic processes is computational expensive. Li et al. (2014) have proposed computationally cheap surrogate models for efficient optimization of SMB chromatography. In this study, only the operating parameters of U_2 are optimized; the operating conditions of U_1 are taken directly from the empirical design. Moreover, only the Pareto optimal fragment with purity higher than 99% is concerned, such that fewer points are requested. The maximal sampling length of MCMC is 300, and the burn-in length is 50. The Pareto front of the cascade scheme is illustrated in Fig. 9. As seen from the Pareto fronts, the cascade scheme outperforms the single column system in both purity and yield indicators.

Three characteristic points (i.e., a, b, c), ranging yields from high to low, on the Pareto front are compared. The corresponding operating conditions are listed in Tab. 6; and the resulting chromatograms are shown in Fig. 10. The combined axial concentration profiles in all columns are displayed at multiples of the switching time. The performance vector $[\mathcal{PI}_{\mathrm{cyt}}^E]_{U_2} = [\mathrm{Pu}_{\mathrm{cyt}}^E, \mathrm{Y}_{\mathrm{cyt}}^E]_{U_2}$ of the point a is [99.27%, 0.96] (cf. Fig. 10a), [99.81%, 0.95] of the point b (cf. Fig. 10b) and [100%, 0.39] of the point c (cf. Fig. 10c). After numerical optimization, the performance indicators tremendously increase from that of the empirical design, [97.92%, 0.33]. The main difference between the chromatograms of a and b is that less RNase keeps retained to port E in b, resulting in higher purity at port E. The productivities of cyt, $[\mathrm{Pr}_{\mathrm{cyt}}^E]_{U_2}$, are $[3.13 \cdot 10^{-4}, 3.15 \cdot 10^{-4}, 1.30 \cdot 10^{-4}] \, \mathrm{mol} \, \mathrm{m}^{-3} \, \mathrm{s}^{-1}$, respectively. It indicates that productivity is high when the concentration values in the shadow areas at port E are high and flat. Though RNase and lyz are treated as impurities in the center-cut separation, they can be withdrawn with high performance indicators in this study. For instance, $[\mathcal{PI}_{\mathrm{RNase}}^R]_{U_2} = [96.14\%, 0.97]$ of the point a, [95.45%, 0.98] of the point b.

The salt profiles, $c_0(t,z)$, along the two IEX-SMB units at time upon CSS, $t=\tau$, are depicted in Fig. 11. In U_1 , the salt concentrations at inlet ports, $[c_0^D, c_0^F]_{U_1}$, used for constructing the two solvent gradients are [290, 420] mol m⁻³ (cf. Fig. 8b). The salt concentrations at the inlet ports of U_2 , $[c_0^D, c_0^F]_{U_2}$, are [206.56, 243.53] mol m⁻³ of the point a; [203.92, 244.93] mol m⁻³ of the point b and [208, 243] mol m⁻³ of the point c.

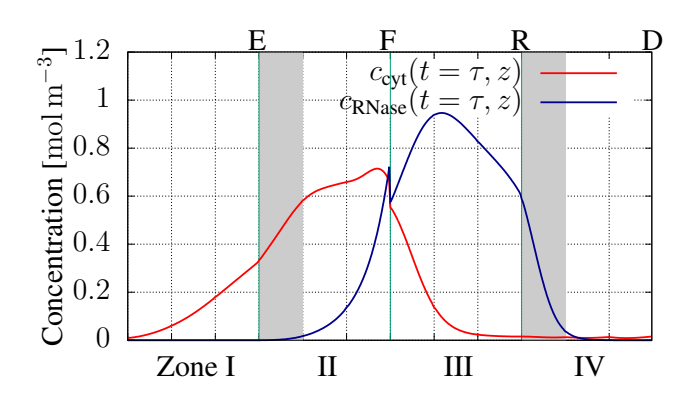
The salt gap of solvent between zones I,II and zones III,IV of U_1 (cf. Fig. 8b) facilitates to separate lyz from the mixture; RNase and cyt are still not rather separated in U_2 . Because of the salt profile in zones III and IV (i.e., ca. $320 \,\mathrm{mol}\,\mathrm{m}^{-3}$), RNase and cyt have approximately the same electrostatic interaction forces with the stationary phase, causing rather similar desorption rates off the stationary phase. In order to separate RNase and cyt in U_2 , the salt concentrations at the inlet ports should be reduced, leading one component (i.e., cyt) to be strongly bounded. This can be achieved by diluting the bypass stream of U_2 with pure buffer (in the cascade scheme, the flow between the raffinate stream of U_1 and feed stream of U_2 is defined as a bypass stream):

$$\left[c_{\text{in},i}^{F}\right]_{U_{2}} = \frac{\left[Q^{R}c_{\text{out},i}^{R}\right]_{U_{1}}}{\left[Q^{R}\right]_{U_{1}} + Q^{\text{dilute}}} \qquad i \in \{0,\dots,M\}$$
(19)

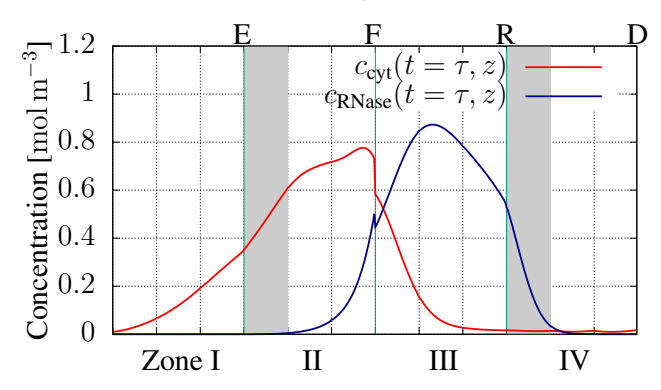
In numerical optimization, $[Q^F]_{U_2}$ and $[Q^R]_{U_1}$ are optimized, $Q^{\text{dilute}} = [Q^F]_{U_2} - [Q^R]_{U_1}$ and $[c_{\text{in},i}^F]_{U_2}$ are subsequently changed. As seen in Fig. 11, the salt concentration in U_2 is decreased to ca. 200 mol m⁻³ in zones I,II and 160 mol m⁻³ in zones III,IV. With these salt concentrations, RNase and cyt can be separated in U_2 . With the dilution, the protein concentrations are decreased as a side effect. Therefore, the peaks in U_2 are not as concentrated as have observed in U_1 ; they distribute over several zones, which makes the process design of the U_2 challenging.

4.3 Eight-zone scheme

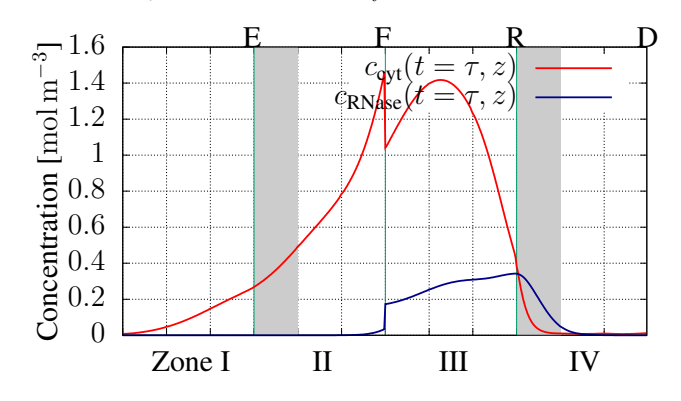
As in the design of the cascade scheme, the initial values were obtained from empirical designs with manual efforts. The searching domain for the numerical optimization is based on the initial values with safety margins, see Tab. 5. The dilution as described in the design of the cascade scheme was applied to the bypass stream (*i.e.*, the connection between the raffinate-I of the first sub-unit and the feed-II of the second







(b)
$$\mathcal{PI}_{\mathrm{cyt}}^E = [99.81\%, 0.95], \Pr_{\mathrm{cyt}}^E = 3.15 \cdot 10^{-4} \, \mathrm{mol} \, \mathrm{m}^{-3} \, \mathrm{s}^{-1}$$



(c)
$$\mathcal{PI}_{\mathrm{cyt}}^E = [100\%, 0.39], \Pr_{\mathrm{cyt}}^E = 1.30 \cdot 10^{-4} \, \mathrm{mol} \, \mathrm{m}^{-3} \, \mathrm{s}^{-1}$$

Figure 10: Chromatograms of the second sub-unit in the cascade IEX-SMB upon CSS from numerical optimization.

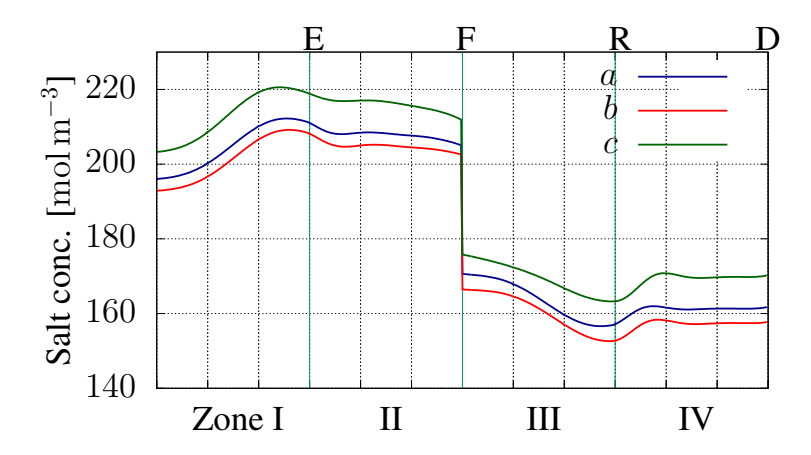


Figure 11: Salt profiles, $c_0(t, z)$, along the columns of the cascade scheme upon the CSS $(t = \tau)$ from the numerical optimization.

Table 5:	Searching	domain	for t	he design	of eight-zone	scheme.

Symbol	Description —	Value	Unit	
Symbol	Description —	min	max	Onic
t_s	switch time	90	110	s
Q^{rec}	recycle flowrate	$2.0 \cdot 10^{-8}$	$2.5 \cdot 10^{-8}$	${ m m}^{3}{ m s}^{-1}$
Q^{D1}	desorbent one flowrate	$0.94 \cdot 10^{-8}$	$1.14 \cdot 10^{-8}$	${ m m}^{3}{ m s}^{-1}$
Q^{E1}	extract one flowrate	$0.99 \cdot 10^{-8}$	$1.19 \cdot 10^{-8}$	${ m m}^{3}{ m s}^{-1}$
Q^{F1}	feed one flowrate	$0.45 \cdot 10^{-8}$	$0.65 \cdot 10^{-8}$	${ m m}^{3}{ m s}^{-1}$
Q^{R1}	raffinate one flowrate	$0.50 \cdot 10^{-8}$	$0.70 \cdot 10^{-8}$	${ m m}^{3}{ m s}^{-1}$
Q^{D2}	desorbent two flowrate	$1.30 \cdot 10^{-8}$	$1.55 \cdot 10^{-8}$	${ m m}^{3}{ m s}^{-1}$
Q^{E2}	extract two flowrate	$1.09 \cdot 10^{-8}$	$1.29 \cdot 10^{-8}$	${ m m}^{3}{ m s}^{-1}$
Q^{F2}	feed two flowrate	$0.65 \cdot 10^{-8}$	$0.85 \cdot 10^{-8}$	${ m m}^{3}{ m s}^{-1}$
c_0^{F1}	feed one salt conc.	270	310	$\rm molm^{-3}$
c_0^{D1}	desorbent one salt conc.	410	450	$\rm molm^{-3}$
c_0^{F2}	feed two salt conc.	170	220	$\rm molm^{-3}$
$Q^{F2} \\ c_0^{F1} \\ c_0^{D1} \\ c_0^{F2} \\ c_0^{F2} \\ c_0^{D2}$	desorbent two salt conc.	240	260	$ m molm^{-3}$

sub-unit). With the operating conditions listed in the *empirical* column of Tab. 7, cyt spreads from zone VI to zone VII, RNase from zone V to VI, such that $Pu_{RNase}^{R2} = 73.23\%$ and $Pu_{cyt}^{E2} = 87.50\%$ (the chromatogram is not shown).

In this case, a total of ca. k=148 switches was required for each eight-zone simulation to fall below the tolerance error of $e_t=10^{-5}$. The convergence time from an initial state to the CSS, thus the total computational time, in the eight-zone scheme is longer than that in the cascade scheme. The maximal sampling length of MCMC is 300, and the burn-in length is 50. The Pareto optimal front with purity larger than 99% is illustrated in Fig. 12; the Pareto fronts of single column and cascade systems are superimposed for comparison. The shadow areas of light blue show the sampling region.

By using the multi-objective sampling algorithm, MCMC, not only the Pareto front solutions but also the points near Pareto front can be studied. In this study, three points (i.e., a, b, c; the point c is on the Pareto front), ranging purities from low to high, were chosen to illustrate the impact of the composition of R1 stream on the performance of the second sub-unit. The corresponding operating conditions are listed in Tab. 7; and the chromatograms upon CSS are shown in Fig. 13. The combined axial concentration profiles in all columns are displayed at multiples of the switching time. In Fig. 13a, cyt is collected at the E2 node with $\mathcal{PI}_{\text{cyt}}^{E2} = [97.18\%, 0.95]$, while [98.98%, 0.90] in Fig. 13b and [99.27%, 0.97] in Fig. 13c. As seen from Fig. 13, the higher concentration of the cyt composition in the R1 stream, the higher of the yield and productivity

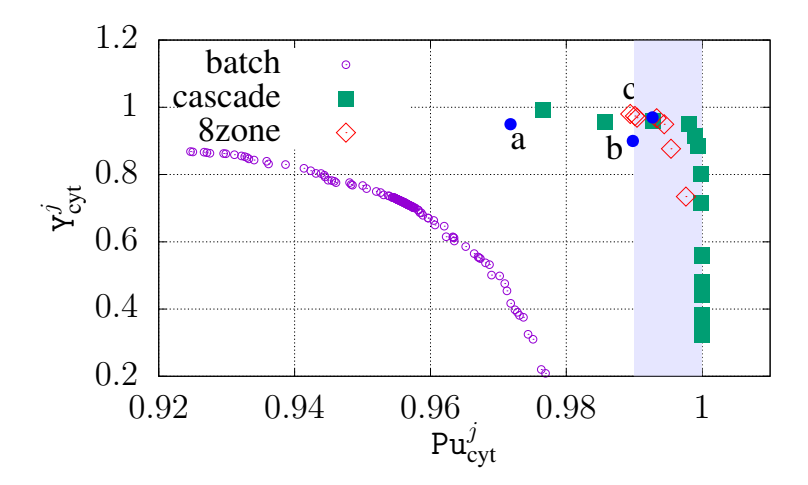


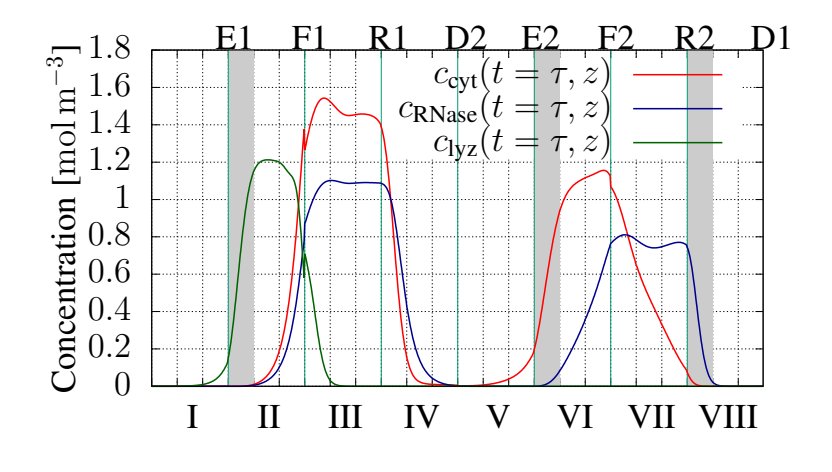
Figure 12: Pareto front of the purity and yield performance indicators of the eight-zone scheme.

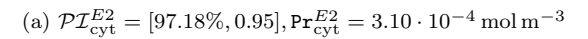
indicators at the E2 port. To be specific, $\mathbf{Y}^{E2}_{\mathrm{cyt}}=0.95$ and $\mathbf{Pr}^{E2}_{\mathrm{cyt}}=3.10\,\mathrm{mol\,m^{-3}\,s^{-1}}$ of the point $a;\,\mathbf{Y}^{E2}_{\mathrm{cyt}}=0.90$ and $\mathbf{Pr}^{E2}_{\mathrm{cyt}}=2.93\,\mathrm{mol\,m^{-3}\,s^{-1}}$ of the point $b,\,\mathrm{and}\,\,\mathbf{Y}^{E2}_{\mathrm{cyt}}=0.97$ and $\mathbf{Pr}^{E2}_{\mathrm{cyt}}=3.25\,\mathrm{mol\,m^{-3}\,s^{-1}}$ of the point $c.\,\mathrm{Although}$ in the center-cut separation, the other two components (i.e., RNase and lyz) can be viewed as impurities, they can rather be withdrawn with high performance indicators. Specifically, for RNase at the R2 node it is $\mathcal{PI}^{R2}_{\mathrm{RNase}}=[94.86\%,0.97]$ of the point $a,\,[91.80\%,0.99]$ of the point $b,\,[99.94\%,1.00]$ of the point $b,\,[99.94\%,1.00]$

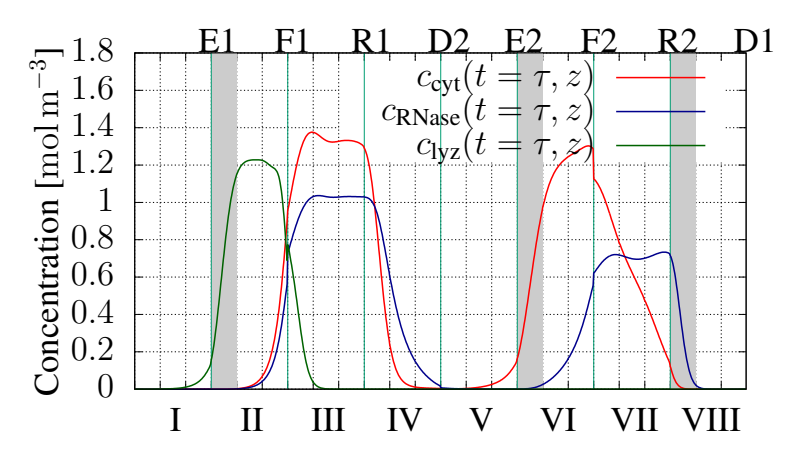
The salt profile, $c_0(t,z)$, along the eight-zone IEX-SMB unit at time upon CSS, $t=\tau$, are attached in Fig. 14. The salt concentrations at inlet ports, $[c_0^{D1}, c_0^{F1}, c_0^{D2}, c_0^{F2}]$, are $[442, 270, 240, 211] \,\mathrm{mol}\,\mathrm{m}^{-3}$ of the point a; $[440, 270, 240, 209] \,\mathrm{mol}\,\mathrm{m}^{-3}$ of the point b and $[443, 272, 240, 217] \,\mathrm{mol}\,\mathrm{m}^{-3}$ of the point c. Separating lyz at port E1 is facilitated with the salt gap between zones I,II and zones III,IV; RNase and cyt are both weekly bounded in zones III,IV and to be separated in the second sub-unit. Meanwhile, the bypass stream was diluted as described by Eq. 19. As seen in Fig. 14, the salt concentration is decreased to ca. 240 $\,\mathrm{mol}\,\mathrm{m}^{-3}$ in zones V,VI and 220 $\,\mathrm{mol}\,\mathrm{m}^{-3}$ in zones III,IV. With these salt concentrations, RNase is weakly bounded and cyt is strongly bounded in the second sub-unit. As seen from Fig. 14, the deviation of the salt profile along the columns of IEX-SMB is small, but the performance indicators varied. This indicates process design of IEX-SMB processes is sensitive to operating conditions.

Eight-zone schemes have fewer degrees of freedom than cascade schemes. Hence, Pu_{cyt}^{E2} decreases from 99.81% of the cascade scheme to 97.18%, based on the same yield, 0.95. Moreover, in the cascade scheme, almost pure cyt can be collected, which can not be achieved with the eight-zone scheme. However, the productivity of the eight-zone scheme can be higher than that of the cascade scheme. The productivity of the cascade scheme, $3.13 \cdot 10^{-4} \text{ mol m}^{-3} \text{ s}^{-1}$ ($\mathcal{PI}_{\text{cyt}}^{E2} = [99.27\%, 0.96]$), is slightly lower than that of the eight-zone scheme, $3.25 \cdot 10^{-4} \text{ mol m}^{-3} \text{ s}^{-1}$ ($\mathcal{PI}_{\text{cyt}}^{E2} = [99.27\%, 0.97]$). This suggests that the stationary phase is more efficiently utilized with integrated SMB processes.

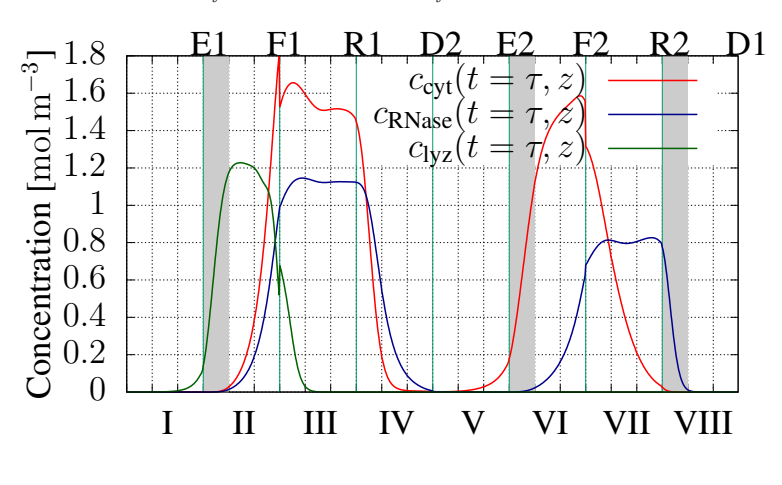
Three columns in each zone was chosen and used in both the cascade and eight-zone schemes. In the empirical designs, neither one column nor two columns in each zone could lead to good separation performance. Having more columns in each zone and less switching time can approximate the true moving bed chromatography. However, introducing more columns into IEX-SMB system makes challenges for computational resource. Three columns in each zone is a good compromise.







(b)
$$\mathcal{PI}_{\mathrm{cyt}}^{E2} = [98.98\%, 0.90], \Pr_{\mathrm{cyt}}^{E2} = 2.93 \cdot 10^{-4} \, \mathrm{mol} \, \mathrm{m}^{-3}$$



(c)
$$\mathcal{PI}_{\mathrm{cyt}}^{E2} = [99.27\%, 0.97], \Pr_{\mathrm{cyt}}^{E2} = 3.25 \cdot 10^{-4} \, \mathrm{mol} \, \mathrm{m}^{-3}$$

Figure 13: Chromatograms of the eight-zone IEX-SMB upon CSS from numerical optimization.

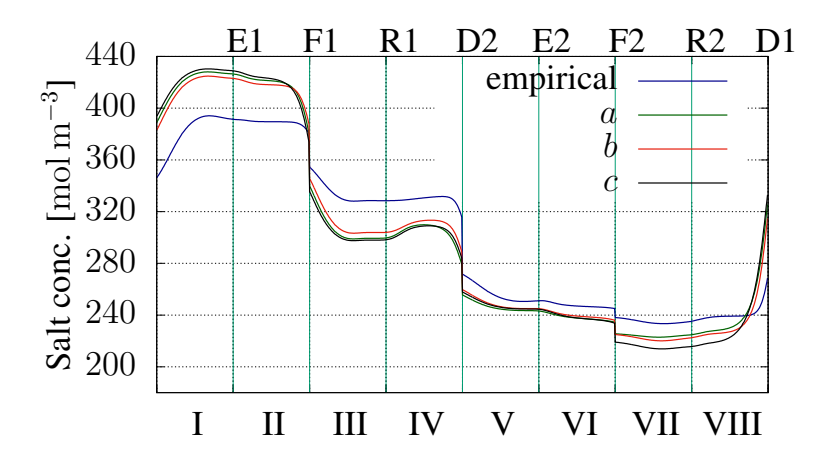


Figure 14: The actual salt profiles, $c_0(t = \tau, z)$, along the columns of the eight-zone scheme upon the CSS by controlling solvent gradients at inlet ports.

Table 6: Operating parameters of the point a,b,c in the cascade IEX-SMB units.

Symbol	Description —	Empirical		Numerical			- Unit
	Description —	U_1	U_2	a	b	c	- Ont
Q^F	feed flowrate	$0.55 \cdot 10^{-8}$	$0.75 \cdot 10^{-8}$	$1.48 \cdot 10^{-8}$	$1.37 \cdot 10^{-8}$	$1.56 \cdot 10^{-8}$	${\rm m}^{3}{\rm s}^{-1}$
Q^R	raffinate flowrate	$0.60 \cdot 10^{-8}$	$0.90 \cdot 10^{-8}$	$1.49 \cdot 10^{-8}$	$1.36 \cdot 10^{-8}$	$1.63 \cdot 10^{-8}$	${ m m}^{3}{ m s}^{-1}$
Q^D	desorbent flowrate	$1.14 \cdot 10^{-8}$	$1.34 \cdot 10^{-8}$	$1.24 \cdot 10^{-8}$	$1.22 \cdot 10^{-8}$	$1.24 \cdot 10^{-8}$	${ m m}^{3}{ m s}^{-1}$
Q^E	extract flowrate	$1.09 \cdot 10^{-8}$	$1.19 \cdot 10^{-8}$	$1.23 \cdot 10^{-8}$	$1.22 \cdot 10^{-8}$	$1.17 \cdot 10^{-8}$	${ m m}^{3}{ m s}^{-1}$
Q^{I} Q^{II}	zone I flowrate	$2.21 \cdot 10^{-8}$	$2.56 \cdot 10^{-8}$	$2.96 \cdot 10^{-8}$	$2.90 \cdot 10^{-8}$	$3.01 \cdot 10^{-8}$	${ m m}^{3}{ m s}^{-1}$
Q^{11}	zone II flowrate	$1.12 \cdot 10^{-8}$	$1.37 \cdot 10^{-8}$	$1.73 \cdot 10^{-8}$	$1.63 \cdot 10^{-8}$	$1.84 \cdot 10^{-8}$	${\rm m}^{3}{\rm s}^{-1}$
$Q^{ m III} \ Q^{ m IV}$	zone III flowrate	$1.67 \cdot 10^{-8}$	$2.12 \cdot 10^{-8}$	$3.21 \cdot 10^{-8}$	$3.04 \cdot 10^{-8}$	$3.40 \cdot 10^{-8}$	${\rm m}^{3}{\rm s}^{-1}$
Q^{IV}	zone IV flowrate	$1.07 \cdot 10^{-8}$	$1.22 \cdot 10^{-8}$	$1.72 \cdot 10^{-8}$	$1.69 \cdot 10^{-8}$	$1.77 \cdot 10^{-8}$	${\rm m}^{3}{\rm s}^{-1}$
c_0^F	feed salt conc.	290	200	206.56	203.92	208	$\rm molm^{-3}$
$c_0^F \\ c_0^D$	desorbent salt conc.	420	240	243.53	244.93	243	$\mathrm{mol}\mathrm{m}^{-3}$
t_s	switching time			100			s

Table 7: Operating parameters of the point a, b, c in the eight-zone IEX-SMB

Symbol	Description	Value				TT 14
Symbol	Description —	Empirical	a	b	c	Unit
Q^{F1}	feed one flowrate	$0.477 \cdot 10^{-8}$	$0.544 \cdot 10^{-8}$	$0.544 \cdot 10^{-8}$	$0.554 \cdot 10^{-8}$	${ m m}^{3}{ m s}^{-1}$
Q^{R1}	raffinate one flowrate	$0.518 \cdot 10^{-8}$	$0.586 \cdot 10^{-8}$	$0.574 \cdot 10^{-8}$	$0.558 \cdot 10^{-8}$	${ m m}^{3}{ m s}^{-1}$
Q^{D1}	desorbent one flowrate	$1.086 \cdot 10^{-8}$	$1.072 \cdot 10^{-8}$	$1.082 \cdot 10^{-8}$	$1.089 \cdot 10^{-8}$	${ m m}^{3}{ m s}^{-1}$
Q^{E1}	extract one flowrate	$1.056 \cdot 10^{-8}$	$1.023 \cdot 10^{-8}$	$1.020 \cdot 10^{-8}$	$1.045 \cdot 10^{-8}$	${ m m}^{3}{ m s}^{-1}$
Q^{I}	zone I flowrate	$2.166 \cdot 10^{-8}$	$2.000 \cdot 10^{-8}$	$2.021 \cdot 10^{-8}$	$2.000 \cdot 10^{-8}$	${ m m}^{3}{ m s}^{-1}$
Q_{II}	zone II flowrate	$1.110 \cdot 10^{-8}$	$0.977 \cdot 10^{-8}$	$1.001 \cdot 10^{-8}$	$0.955 \cdot 10^{-8}$	${ m m}^{3}{ m s}^{-1}$
Q^{III}	zone III flowrate	$1.587 \cdot 10^{-8}$	$1.521 \cdot 10^{-8}$	$1.540 \cdot 10^{-8}$	$1.508 \cdot 10^{-8}$	${ m m}^{3}{ m s}^{-1}$
Q^{IV}	zone IV flowrate	$1.069 \cdot 10^{-8}$	$0.935 \cdot 10^{-8}$	$0.966 \cdot 10^{-8}$	$0.950 \cdot 10^{-8}$	${ m m}^{3}{ m s}^{-1}$
O^{F2}	feed two flowrate	$0.753 \cdot 10^{-8}$	$0.826 \cdot 10^{-8}$	$0.837 \cdot 10^{-8}$	$0.843 \cdot 10^{-8}$	${\rm m}^{3}{\rm s}^{-1}$
Q^{R2}	raffinate two flowrate	$1.009 \cdot 10^{-8}$	$1.122 \cdot 10^{-8}$	$1.164 \cdot 10^{-8}$	$1.189 \cdot 10^{-8}$	${\rm m}^{3}{\rm s}^{-1}$
Q^{D2}	desorbent two flowrate	$1.510 \cdot 10^{-8}$	$1.391 \cdot 10^{-8}$	$1.408 \cdot 10^{-8}$	$1.408 \cdot 10^{-8}$	${ m m}^{3}{ m s}^{-1}$
Q^{E2}	extract two flowrate	$1.243 \cdot 10^{-8}$	$1.102 \cdot 10^{-8}$	$1.109 \cdot 10^{-8}$	$1.101 \cdot 10^{-8}$	${\rm m}^{3}{\rm s}^{-1}$
Q^{V}	zone V flowrate	$2.579 \cdot 10^{-8}$	$2.327 \cdot 10^{-8}$	$2.374 \cdot 10^{-8}$	$2.358 \cdot 10^{-8}$	${\rm m}^{3}{\rm s}^{-1}$
Q^{VI}	zone VI flowrate	$1.336 \cdot 10^{-8}$	$1.225 \cdot 10^{-8}$	$1.265 \cdot 10^{-8}$	$1.257 \cdot 10^{-8}$	${\rm m}^{3}{\rm s}^{-1}$
$Q^{ m VII}$	zone VII flowrate	$2.089 \cdot 10^{-8}$	$2.051 \cdot 10^{-8}$	$2.102 \cdot 10^{-8}$	$2.100 \cdot 10^{-8}$	${ m m}^{3}{ m s}^{-1}$
Q^{VII}	zone VIII flowrate	$1.080 \cdot 10^{-8}$	$0.928 \cdot 10^{-8}$	$0.939 \cdot 10^{-8}$	$0.911 \cdot 10^{-8}$	${\rm m}^{3}{\rm s}^{-1}$
c_0^{F1}	feed one salt conc.	295.1	270.0	270.2	270.5	$\rm molm^{-3}$
c_0^{D1}	desorbent one salt conc.	422.0	442.0	440.3	442.7	$\rm molm^{-3}$
c_0^{F2}	feed two salt conc.	183.1	211.0	209.4	216.6	$\rm molm^{-3}$
Q^{VII} c_{0}^{F1} c_{0}^{D1} c_{0}^{F2} c_{0}^{D2}	desorbent two salt conc.	240.7	240.0	240.0	240.5	$\rm molm^{-3}$
t_s	switching time	105.9	109.1	109.8	109.7	s

5 Conclusions

We have presented model-based process designs of multi-step salt gradient single column system and IEX-SMB processes for separating ribonuclease, cytochrome and lysozyme on strong cation-exchanger SP Sepharose FF. The general rate model with steric mass-action binding kinetics was used in the column modelling. Two network configurations of closed-loop IEX-SMB have been studied, *i.e.*, one cascade scheme of two four-zone IEX-SMB sub-units and one integrated eight-zone scheme; the single column batch system has been studied for comparison. The multi-objective sampling algorithm, Markov Chain Monte Carlo (MCMC), has been used to generate samples for approximating the Pareto optimal fronts. This study shows that it is possible to design closed-loop IEX-SMB units for collecting the target, cytochrome.

In the numerical optimizations of IEX-SMB, initial values are required. Empirical rules have been developed in this study to obtain the initial values, and the searching domains of numerical optimization are based on the initial values with safety margins. MCMC serves on the sampling purpose, which is interested in sampling Pareto optimal points as well as those near Pareto optimal. With ε -constraint method of the multi-objective optimization, Pareto optimal fragments can be concerned to reduce expensive computational cost in large-scale IEX-SMB processes. The Pareto fronts show the information of the trade-off relationship between the conflicting indicators (*i.e.*, purity and yield). Although in center-cut separations the other two components (*i.e.*, ribonuclease and lysozyme) are treated as impurities, they can be collected with rather high performance indicators.

As illustrated by the Pareto fronts, the cascade scheme and the eight-zone scheme have approximately the same performance, that both outperforms the single column system with respect to the conflicting performance indicators, *i.e.*, purity and yield. In addition, the cascade scheme can produce almost pure target component with high yield. As seen from the productivity indicators, the stationary phase is more utilized in the integrated eight-zone scheme. However, single column system does not undergo a time-consuming ramp-up phase and eventually enters into a cyclic steady state, like it is in SMB systems. It is also recommended starting a single column batch system prior to complex multi-column and SMB systems.

Dilution steps were applied in the bypass streams of both IEX-SMB schemes to reduce the salt concentrations of the outlet streams of the first sub-unit, leading cytochrome to be strongly bounded in the second sub-unit. Without the dilution steps, the salt concentrations are too high such that ribonuclease and cytochrome are both weekly bounded to the stationary phase of the second sub-unit. Though it is beneficial to implement dilution in the cascade and eight-zone schemes for center-cut separations, it consumes more running buffer on one hand, and the cytochrome product needs to be more concentrated in the subsequent downstream processes on the other hand.

There are many options for modeling mass transfer in a column, e.g., the equilibrium-dispersive model (EDM), the transport-dispersive model (TDM) and the general rate model (GRM) that can be combined with a multitude of binding kinetics. The software package provided in this study is flexible in choosing between various modelling options for the columns and hold-up volumes. SMB processes do not necessarily need equivalent column numbers in each zone. Different column numbers in each zone can be applied, resulting the optimization problem to mixed-integer programming. The computational burden of SMB processes in numerical optimizations can be reduced by optimizing initial states of the involved columns, or by using computationally cheap surrogate models. 3-dimensional Pareto optimal fronts can also be further investigated, taking buffer consumption, productivity or processing time into account.

6 Acknowledgements

This work is partially supported by the China Scholarship Council (CSC, no. 201408310124) and partially by the National Key Research and Development Program of China (NKRDP, grant. 2017YFB0309302).

References

- Angarita, M., Müller-Späth, T., Baur, D., Lievrouw, R., Lissens, G., & Morbidelli, M. (2015). Twin-column CaptureSMB: a novel cyclic process for protein A affinity chromatography. *Journal of Chromatography A*, 1389, 85–95.
- Antos, D., & Seidel-Morgenstern, A. (2001). Application of gradients in the simulated moving bed process. Chemical Engineering Science, 56, 6667–6682.
- Aumann, L., & Morbidelli, M. (2007). A continuous multicolumn countercurrent solvent gradient purification (MCSGP) process. *Biotechnology and Bioengineering*, 98, 1043–1055.
- Barber, J. A., Perkins, J. D., & Sargent, R. W. (1998). Boundary conditions for flow with dispersion. Chemical Engineering Science, 53, 1463–1464.
- Bentley, J., & Kawajiri, Y. (2013). Prediction-correction method for optimization of simulated moving bed chromatography. *AIChE Journal*, 59, 736–746.
- Bentley, J., Li, S., & Kawajiri, Y. (2014). Experimental validation of optimized model-based startup acceleration strategies for simulated moving bed chromatography. *Industrial & Engineering Chemistry Research*, 53, 12063–12076.
- Bochenek, R., Marek, W., Piątkowski, W., & Antos, D. (2013). Evaluating the performance of different multicolumn setups for chromatographic separation of proteins on hydrophobic interaction chromatography media by a numerical study. *Journal of Chromatography A*, 1301, 60–72.
- Brooks, C. A., & Cramer, S. M. (1992). Steric mass-action ion exchange: displacement profiles and induced salt gradients. *AIChE Journal*, 38, 1969–1978.
- Broughton, D. B., & Gerhold, C. G. (1961). Continuous sorption process employing fixed bed of sorbent and moving inlets and outlets. US Patent 2,985,589.
- Carta, G., & Jungbauer, A. (2010). Protein chromatography: process development and scale-up. John Wiley & Sons.
- Charton, F., & Nicoud, R.-M. (1995). Complete design of a simulated moving bed. *Journal of Chromatog-raphy A*, 702, 97–112.
- Clark, A. J., Kotlicki, A., Haynes, C. A., & Whitehead, L. A. (2007). A new model of protein adsorption kinetics derived from simultaneous measurement of mass loading and changes in surface energy. *Langmuir*, 23, 5591–5600.
- Diedrich, J., Heymann, W., Leweke, S., Hunt, S., Todd, R., Kunert, C., Johnson, W., & von Lieres, E. (2017). Multi-state steric mass action model and case study on complex high loading behavior of mab on ion exchange tentacle resin. *Journal of Chromatography A*, 1525, 60–70.
- Dismer, F., & Hubbuch, J. (2010). 3D structure-based protein retention prediction for ion-exchange chromatography. *Journal of Chromatography A*, 1217, 1343–1353.
- Duh, K., Sudoh, K., Wu, X., Tsukada, H., & Nagata, M. (2012). Learning to translate with multiple objectives. In *Proceedings of the 50th Annual Meeting of the Association for Computational Linguistics* (Volume 1: Long Papers) (pp. 1–10).
- Faria, R. P., & Rodrigues, A. E. (2015). Instrumental aspects of simulated moving bed chromatography. Journal of Chromatography A, 1421, 82–102.
- Geweke, J. et al. (1991). Evaluating the accuracy of sampling-based approaches to the calculation of posterior moments volume 196. Federal Reserve Bank of Minneapolis, Research Department Minneapolis, MN.

- Ghosh, P., Lin, M., Vogel, J. H., Choy, D., Haynes, C., & von Lieres, E. (2014). Zonal rate model for axial and radial flow membrane chromatography, part ii: Model-based scale-up. *Biotechnology and bioengineering*, 111, 1587–1594.
- Ghosh, P., Vahedipour, K., Lin, M., Vogel, J. H., Haynes, C. A., & von Lieres, E. (2013). Zonal rate model for axial and radial flow membrane chromatography. part i: Knowledge transfer across operating conditions and scales. *Biotechnology and bioengineering*, 110, 1129–1141.
- Guiochon, G., Felinger, A., & Shirazi, D. G. (2006). Fundamentals of preparative and nonlinear chromatography. Academic Press.
- He, Q.-L., Leweke, S., & von Lieres, E. (2018). Efficient numerical simulation of simulated moving bed chromatography with a single-column solver. Computers & Chemical Engineering, 111, 183–198.
- Houwing, J., van Hateren, S. H., Billiet, H. A., & van der Wielen, L. A. (2002). Effect of salt gradients on the separation of dilute mixtures of proteins by ion-exchange in simulated moving beds. *Journal of Chromatography A*, 952, 85–98.
- Houwing, J., Jensen, T. B., van Hateren, S. H., Billiet, H. A., & van der Wielen, L. A. (2003). Positioning of salt gradients in ion-exchange SMB. *AIChE Journal*, 49, 665–674.
- Kazi, M.-K., Medi, B., & Amanullah, M. (2012). Optimization of an improved single-column chromatographic process for the separation of enantiomers. *Journal of Chromatography A*, 1231, 22–30.
- Kim, K.-M., Song, J.-Y., & Lee, C.-H. (2016). Combined operation of outlet streams swing with partial-feed in a simulated moving bed. *Korean Journal of Chemical Engineering*, 33, 1059–1069.
- Kiwala, D., Mendrella, J., Antos, D., & Seidel-Morgenstern, A. (2016). Center-cut separation of intermediately adsorbing target component by 8-zone simulated moving bed chromatography with internal recycle. *Journal of Chromatography A*, 1453, 19–33.
- Lang, K. M., Kittelmann, J., Dürr, C., Osberghaus, A., & Hubbuch, J. (2015). A comprehensive molecular dynamics approach to protein retention modeling in ion exchange chromatography. *Journal of Chromatog-raphy A*, 1381, 184–193.
- Li, P., Xiu, G., & Rodrigues, A. E. (2007). Proteins separation and purification by salt gradient ion-exchange SMB. *AIChE Journal*, 53, 2419–2431.
- Li, S., Feng, L., Benner, P., & Seidel-Morgenstern, A. (2014). Using surrogate models for efficient optimization of simulated moving bed chromatography. Computers & Chemical Engineering, 67, 121–132.
- Liang, J., Fieg, G., Keil, F. J., & Jakobtorweihen, S. (2012). Adsorption of proteins onto ion-exchange chromatographic media: A molecular dynamics study. *Industrial & Engineering Chmistry Research*, 51, 16049–16058.
- Lim, Y.-I. (2004). An optimization strategy for nonlinear simulated moving bed chromatography: multi-level optimization procedure (MLOP). Korean Journal of Chemical Engineering, 21, 836–852.
- Lodi, G., Storti, G., Pellegrini, L. A., & Morbidelli, M. (2017). Ion exclusion chromatography: model development and experimental evaluation. *Industrial & Engineering Chemistry Research*, 56, 1621–1632.
- Marler, R. T., & Arora, J. S. (2010). The weighted sum method for multi-objective optimization: new insights. Structural and multidisciplinary optimization, 41, 853–862.
- Mavrotas, G. (2009). Effective implementation of the ε -constraint method in multi-objective mathematical programming problems. Applied mathematics and computation, 213, 455–465.

- Mazzotti, M., Storti, G., & Morbidelli, M. (1997). Optimal operation of simulated moving bed units for nonlinear chromatographic separations. *Journal of Chromatography A*, 769, 3–24.
- Ng, C. K., Rousset, F., Valery, E., Bracewell, D. G., & Sorensen, E. (2014). Design of high productivity sequential multi-column chromatography for antibody capture. *Food and Bioproducts Processing*, 92, 233–241.
- Nicolaos, A., Muhr, L., Gotteland, P., Nicoud, R.-M., & Bailly, M. (2001). Application of equilibrium theory to ternary moving bed configurations (four+four, five+four, eight and nine zones): I. Linear case. *Journal of Chromatography A*, 908, 71–86.
- Nowak, J., Antos, D., & Seidel-Morgenstern, A. (2012). Theoretical study of using simulated moving bed chromatography to separate intermediately eluting target compounds. *Journal of Chromatography A*, 1253, 58–70.
- Osberghaus, A., Hepbildikler, S., Nath, S., Haindl, M., von Lieres, E., & Hubbuch, J. (2012a). Determination of parameters for the steric mass action model—A comparison between two approaches. *Journal of Chromatography A*, 1233, 54–65.
- Osberghaus, A., Hepbildikler, S., Nath, S., Haindl, M., Von Lieres, E., & Hubbuch, J. (2012b). Optimizing a chromatographic three component separation: A comparison of mechanistic and empiric modeling approaches. *Journal of Chromatography A*, 1237, 86–95.
- Pollock, J., Bolton, G., Coffman, J., Ho, S. V., Bracewell, D. G., & Farid, S. S. (2013). Optimising the design and operation of semi-continuous affinity chromatography for clinical and commercial manufacture. *Journal of Chromatography A*, 1284, 17–27.
- Püttmann, A., Schnittert, S., Naumann, U., & von Lieres, E. (2013). Fast and accurate parameter sensitivities for the general rate model of column liquid chromatography. *Computers & Chemical Engineering*, 56, 46–57.
- Rajendran, A., Paredes, G., & Mazzotti, M. (2009). Simulated moving bed chromatography for the separation of enantiomers. *Journal of Chromatography A*, 1216, 709–738.
- Scopes, R. K. (2013). Protein purification: principles and practice. Springer Science & Business Media.
- Seidel-Morgenstern, A., Kessler, L. C., & Kaspereit, M. (2008). New developments in simulated moving bed chromatography. *Chemical Engineering & Technology*, 31, 826–837.
- da Silva, F. V. S., & Seidel-Morgenstern, A. (2016). Evaluation of center-cut separations applying simulated moving bed chromatography with 8 zones. *Journal of Chromatography A*, 1456, 123–136.
- Silva, M. S., Rodrigues, A. E., & Mota, J. P. (2015). Modeling and simulation of an industrial-scale parex process. *AIChE Journal*, 61, 1345–1363.
- Silva, R. J., Rodrigues, R. C., Osuna-Sanchez, H., Bailly, M., Valéry, E., & Mota, J. P. (2010). A new multicolumn, open-loop process for center-cut separation by solvent-gradient chromatography. *Journal of Chromatography A*, 1217, 8257–8269.
- Sreedhar, B., Hobbs, D. T., & Kawajiri, Y. (2014). Simulated moving bed chromatography designs for lanthanide and actinide separations using Reillex HPQTM resin. Separation and Purification Technology, 136, 50–57.
- Storti, G., Mazzotti, M., Morbidelli, M., & Carrà, S. (1993). Robust design of binary countercurrent adsorption separation processes. *AIChE Journal*, 39, 471–492.

- Teske, C. A., Lieres, E. v., Schröder, M., Ladiwala, A., Cramer, S. M., & Hubbuch, J. J. (2006). Competitive adsorption of labeled and native protein in confocal laser scanning microscopy. *Biotechnology and bioengineering*, 95, 58–66.
- Toumi, A., Engell, S., Diehl, M., Bock, H. G., & Schlöder, J. (2007). Efficient optimization of simulated moving bed processes. *Chemical Engineering and Processing: Process Intensification*, 46, 1067–1084.
- Wooley, R., Ma, Z., & Wang, N.-H. L. (1998). A nine-zone simulating moving bed for the recovery of glucose and xylose from biomass hydrolyzate. *Industrial & Engineering Chemistry Research*, 37, 3699–3709.